MICROSCOPY Highlights

Microscopy, 2015, 409–418
doi: 10.1093/jmicro/dfv053
Advance Access Publication Date: 7 September 2015

Article

Quantitative annular dark-field imaging of single-layer graphene—II: atomic-resolution image contrast

Shunsuke Yamashita[1,2,*], Shogo Koshiya[1], Takuro Nagai[1], Jun Kikkawa[1], Kazuo Ishizuka[1,3], and Koji Kimoto[1,2,*]

[1]Surface Physics and Structure Unit, National Institute for Materials Science, 1-1 Namiki, Tsukuba, Ibaraki 305-0044, Japan, [2]Department of Applied Chemistry, Kyushu University, 1-1 Namiki, Tsukuba, Ibaraki 305-0044, Japan, and [3]HREM Research Inc., 14-48 Matsukazedai, Higashimatsuyama, Saitama 355-0055, Japan

*To whom correspondence should be addressed. E-mail: yamashita.shunsuke@nims.go.jp (S.Y.)/kimoto.koji@nims.go.jp (K.K.)

Received 28 July 2015; Accepted 13 August 2015

Abstract

We have investigated how accurately atomic-resolution annular dark-field (ADF) images match between experiments and simulations to conduct more reliable crystal structure analyses. Quantitative ADF imaging, in which the ADF intensity at each pixel represents the fraction of the incident probe current, allows us to perform direct comparisons with simulations without the use of fitting parameters. Although the conventional comparison suffers from experimental uncertainties such as an amorphous surface layer and specimen thickness, in this study we eliminated such uncertainties by using a single-layer graphene as a specimen. Furthermore, to reduce image distortion and shot noises in experimental images, multiple acquisitions with drift correction were performed, and the atomic ADF contrast was quantitatively acquired. To reproduce the experimental ADF contrast, we used three distribution functions as the effective source distribution in simulations. The optimum distribution function and its full-width at half-maximum were evaluated by measuring the residuals between the experimental and simulated images. It was found that the experimental images could be explained well by a linear combination of a Gaussian function and a Lorentzian function with a longer tail than the Gaussian function.

Key words: STEM, ADF, quantitative analysis, graphene, image simulation, effective source distribution

Introduction

One of the ultimate goals in electron microscopy is the atom-by-atom analysis of materials. Annular dark-field (ADF) imaging [1] in aberration-corrected scanning transmission electron microscopy (STEM) is the most promising technique for achieving this goal because of its intrinsic potential for quantitative structural analysis to determine the locations and elements of atoms in specimens. In fact, quantitative analyses have been performed by the direct comparison of ADF images obtained by experiments and simulations [2–5]. Furthermore, recent advances in aberration correction, which enable us to utilize a finer electron

probe with a high probe current, have made quantitative ADF imaging a practical approach to achieving the goal.

Crystal structure analysis using ADF images relies on a comparison between experiments and simulations; therefore, it is an essential prerequisite that image simulations quantitatively reproduce experimental results. LeBeau and Stemmer [2] first demonstrated the quantification of ADF images, in which the ADF image intensity is normalized by the incident probe current, and that quantified images can be compared with simulated images without arbitrary coefficients. Ishikawa *et al.* reported a quantification method that involved counting the number of electrons using a calibrated ADF detector [3]. We developed a quantification procedure that fully implements the nonlinear response of the signal detection system [4]. To enable quantitative acquisition and comparison, it is essential to remove uncertainties in specimens such as a damaged surface layer and specimen thickness. In our previous study [4], we used a graphene as a specimen to avoid these uncertainties and demonstrated that the mean ADF intensity in an experimental image exhibits good agreement with that in a simulated image.

To achieve atom-by-atom analysis, it is necessary to compare not only mean intensities but also atomic-resolution intensity profiles in ADF images, which are more sensitive to the experimental conditions. This is because the intensity profiles in the case of high-resolution ADF imaging are greatly affected by aberrations of the probe-forming lens system, the defocus spread and the effective source distribution. In particular, the effective source distribution is considered to be a dominant factor determining the contrast in ADF imaging and other elemental analyses [6–8]. A Gaussian function is most commonly assumed for the effective source distribution, and quantitative agreement between Gaussian-convolved and experimental images has been reported in previous studies [3,5,9–13]. On the other hand, a few studies have suggested that the actual distributions have longer tails than the Gaussian function on the basis of the measurements of interference fringes in diffraction patterns [6,14,15]. Although quantitative ADF imaging has often been discussed in terms of visibility (maximum and minimum ADF intensities), atomic intensity profiles have not been fully discussed owing to various experimental difficulties such as the specimen uncertainties and the low quality of ADF images.

In this study, we acquired quantitative atomic-resolution ADF images of a single-layer graphene and compared them with simulated images. The experimental conditions that affect atomic-resolution images excluding the effective source distribution were individually estimated, and the measured parameters were used in STEM simulations. To reduce image distortion and shot noises in experimental images, multiple acquisitions with drift correction were performed using customized scripts. The effects of the effective source distribution were investigated, where Gaussian and other distribution functions with longer tails were assumed and each of them was convolved with the simulated images. We evaluated how accurately the simulated images convolved with each distribution function explain the experimental images, and the most appropriate distribution function for the effective source distribution is discussed on the basis of the root mean square (RMS) of the residuals between experimental and simulated images.

Methods

Acquisition of atomic-resolution ADF images of single-layer graphene

A Titan^3 microscope (FEI) equipped with a high-brightness Schottky emission gun (X-FEG) and tandem spherical-aberration correctors (DCOR and CETCOR, CEOS) was used at an accelerating voltage of 80 kV. The DCOR probe corrector was carefully aligned to minimize the fifth-order spherical-aberration coefficient by the manufacturer. A single-layer graphene was used as a specimen because of its clear structure. The convergence semi-angle of the incident probe was 29 mrad. The camera length was set at 145 mm, which corresponds to the detection semi-angle range of the ADF detector (Model 3000, Fischione) of 48.4–200 mrad. The inner angle corresponding to the edge of the scintillator cannot be measured by observing the shadow of the ADF detector owing to the metal pipe at the inner edge of the ADF detector [2]. Therefore, the inner angle was precisely measured by scanning the probe on the ADF detector in the TEM imaging mode. Furthermore, the outer angle does not correspond to the physical size of the ADF detector since scattered electrons at high angles are blocked by an aperture before reaching the ADF detector. Therefore, we measured the outer angle by tracking the highest angle at which diffraction intensities were detectable using an objective aperture for an image-forming lens (for details of the measurement, see our previous article [4]). The basic microscope settings were controlled using Titan^3 control software, and ADF images were acquired using DigiScan II and DigitalMicrograph (Gatan). The incident probe current of a few tens of picoamperes was controlled by varying the gun lens and measured using a bottom-mount charge-coupled device camera, whose conversion efficiency had been calibrated. Because of the small scattering cross section of a single-layer graphene, the mean ADF intensity is only ~0.05% of that of the incident electrons [4]. We acquired images using customized DigitalMicrograph scripts for multiple fast acquisitions and drift correction to improve the signal-to-noise (S/N) ratio and reduce image distortion due to specimen drift [16–18]. The dwell time of each image was set at 0.02 ms

per pixel and 300 ADF images were acquired. After the acquisition, the specimen drift in the images was measured and corrected, and a summed ADF image was obtained. The obtained ADF image was converted into a quantitative ADF image using our quantification procedure [4], which fully corrects the nonlinear response of the signal detection system using an empirical equation. The converted ADF intensities, which are fractions of the incident probe intensity, are called the quantitative contrast Q_{ADF} in this study.

Multislice image simulation with effective source distribution

The STEM image simulation was performed using a multislice program (xHREM with STEM Extension, HREM Research Inc.), which includes the absorptive potential for thermal diffuse scattering proposed by Weickenmeier and Kohl [19,20]. The thermal factor B in the Debye–Waller factor was set to 1.0×10^3 pm^2 [21]. It is worth mentioning that the thermal factor B affects intensities of both elastic scattering and thermal diffuse scattering, but the total intensity is not strongly dependent on B in the case of a single-layer graphene. The basic simulation conditions were adjusted to match the experimental conditions. The coefficients of residual geometrical aberrations up to the fifth order were measured using the probe corrector software (CEOS), and they were incorporated into the simulations except for the defocus and 2-fold astigmatism, because these low-order aberrations are time-dependent and usually optimized just before each image acquisition. The defocus spread due to the chromatic aberration was calculated to be 20 nm using Eq. (1), in which the chromatic aberration coefficient C_C of the probe-forming lens system including the probe corrector was 1.8 mm and the energy spread ΔE of the incident electrons was 0.9 eV.

$$\text{Defocus spread} = C_C \frac{\Delta E}{E}. \quad (1)$$

To incorporate the effect of the defocus spread into the simulations, the defocused images at 1 nm intervals were simulated, and a Gaussian weighted-average image was obtained. The defocus in the experiments was adjusted using a Ronchigram, and the deviation from the in-focus condition was negligible compared with the defocus spread.

Subsequently, the effective source distribution was incorporated into the simulated images. The effective source distribution is defined as the incoherent spread of the probe from a point source due to various effects such as the physical size of the electron source, mechanical and electrical instabilities in the probe-forming lens system and specimen drift. The effects can be incorporated by convolution with a kernel that corresponds to the effective source distribution. In this study, we used three distribution functions as the effective source distribution: Gaussian, Lorentzian (bivariate Cauchy) and their linear combination (Gaussian + Lorentzian). These functions are described in detail in 'Results and discussion' section.

Quantitative comparison between experimental and simulated images

Prior to comparing the experimental and simulated images in detail, the full-width at half-maximum (FWHM) of each effective source distribution was optimized by measuring the RMS of the residuals between the experimental and convolved images. Here, the residual means the difference in the quantitative contrast Q_{ADF} between experimental and simulated images convolved with the effective source distribution. During the FWHM optimization, the FWHM for each distribution function was varied between 10 and 200 pm at 10 pm intervals. An area (0.83×0.99 nm^2) of the experimental images was used for residual measurements. It should be noted that no affine transformation or smoothing of the experimental images was performed, but the convolved images were transformed to align them with sub-pixel accuracy, so that inherent shot noises were retained. As reported in our previous article [4], the mean quantitative contrast Q_{ADF} showed good agreement between experiments and simulations. However, slight discrepancy corresponding to ~2–3% of the mean values was observed in the experimental images, which may result from the non-uniformity of the ADF detector sensitivity [2,22] or measurement errors of the probe current. For these reasons, we slightly adjusted the mean values of the convolved images by multiplying the coefficients to correct the 2–3% differences. Then, the convolved images with the optimum FWHM for each distribution function were compared with the experimental images in detail.

Results and discussion

Figure 1a and b shows experimental ADF images of a single-layer graphene. The quantitative contrast scale is shown on the right side. These two images were acquired with different probe currents of (a) 26.1 pA and (b) 98.9 pA keeping other experimental imaging conditions the same. These images were obtained by summing 300 and 251 images for (a) and (b), respectively. Some of the images acquired with the higher probe current were not used because of knock-on damage during the multiple acquisitions. The 0.14-nm-spaced carbon atoms are clearly resolved in both experimental images. Moreover, the {200} spots, corresponding to a spatial frequency of $(0.1066\ \text{nm})^{-1}$, are also clearly observed in their Fourier transforms shown in the insets. Because the experimental image in (b) was acquired with an

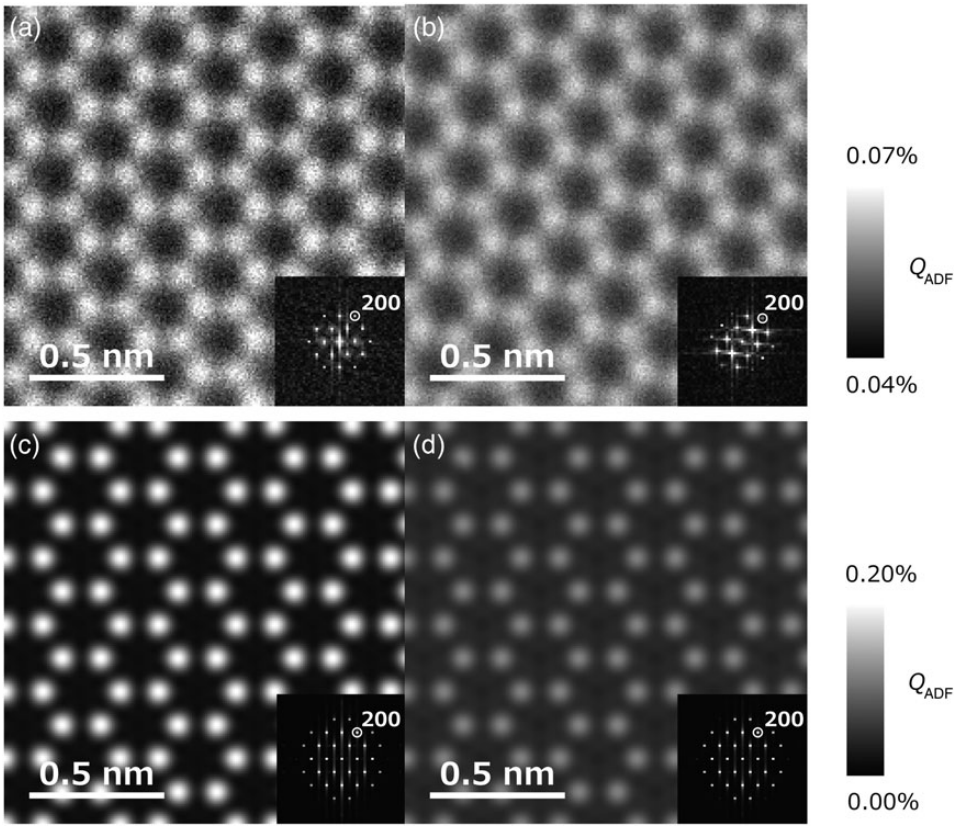

Fig. 1. Experimental ADF images of single-layer graphene acquired with (a) lower probe current of 26.1 pA and (b) higher probe current of 98.9 pA. Simulated images of single-layer graphene (c) without and (d) with incorporating the defocus spread. The brightness of the images is given as the quantitative contrast Q_{ADF}, which is the fraction of the incident probe intensity. The quantitative contrast scales for the experimental and simulated images are set in the ranges of 0.04–0.07 and 0.00–0.20%, respectively. The corresponding Fourier transforms are shown in the insets. Image simulation conditions, such as aberrations and the defocus spread of the probe-forming lens, were adjusted to match the experimental conditions, although the effective source distribution was not taken into account.

electron dose of ~3.2 times larger than that used for (a), the shot noises in (b) appear to be small, i.e., the S/N ratio in (b) is higher than that in (a). On the other hand, the image visibility in (b) appears to be lower than that in (a). Figure 1c and d shows simulated images of a single-layer graphene without and with the incorporation of the defocus spread, respectively. The quantitative contrast scale is also shown on the right side. The ranges of the quantitative contrast Q_{ADF} are 0.01–0.20% for (c) and 0.03–0.11% for (d). Thus, including the defocus spread (temporal partial coherence) into the simulation leads to a large reduction in image visibility. However, the visibility of the simulated image in Fig. 1d is still higher than that of the experimental images (see the quantitative contrast range). This is because the image simulation was performed assuming a point electron source, namely a perfect spatial coherence. Thus, the next step is to take into account an effective source distribution (spatial partial coherence) in simulations in order to quantitatively reproduce experiments.

Figure 2 indicates the three distribution functions, i.e., Gaussian, Lorentzian (bivariate Cauchy) and their linear combination (Gaussian + Lorentzian) [15], each with an FWHM of 100 pm.

They are defined in Eqs. (2)–(4), where R and F represent the distance from the origin and the FWHM, respectively. It should be noted that Eq. (3) represents the two-dimensional Lorentzian [8,15], not the one-dimensional Lorentzian that is nonintegrable in two dimensions [6]. The coefficient f_L denotes a fraction of the Lorentzian and can be given an arbitrary value between 0 and 1. For simplicity, f_L was fixed at 0.5 and the common FWHM was applied to both Gaussian and Lorentzian in the Gaussian + Lorentzian function in this study.

$$\text{Gaussian}\,(R) = \frac{4\ln 2}{\pi F^2}\exp\left[-4\ln 2\left(\frac{R}{F}\right)^2\right], \tag{2}$$

$$\text{Lorentzian}\,(R) = \frac{F}{4\pi\sqrt{\sqrt[3]{4}-1}}\frac{1}{\left(R^2+\dfrac{F^2}{4(\sqrt[3]{4}-1)}\right)^{\frac{3}{2}}}, \tag{3}$$

$$\begin{aligned}\text{G}+\text{L}(R) = {} & (1-f_L)(\text{Gaussian}\,(R)) \\ & + f_L(\text{Lorentzian}\,(R))\,.\end{aligned} \tag{4}$$

As shown in Fig. 2, the Gaussian and Lorentzian functions have shorter and longer tails, respectively, while the Gaussian + Lorentzian function has an intermediate shape between these functions. Increasing the tail length leads to a decrease in the peak height. These differences in shape substantially affect the visibility of ADF images.

Next, we optimize the FWHM of each distribution function to minimize the difference between the experimental and convolved images. The RMS of the residuals between the experimental and convolved images is shown as a function of the FWHM in Fig. 3, where the vertical axes are shown with a logarithmic scale to accentuate the differences between the functions. Figure 3a and b corresponds to the lower (26.1 pA) and higher (98.9 pA) probe currents, respectively, in which the optimum FWHM for each function and the corresponding RMS of the residuals are tabulated in the insets. In the case of the Gaussian function, the RMS of the residuals at the optimum FWHM has a larger value than those of the other two functions. This indicates that the experimental images are not reproduced optimally using the Gaussian function, even though the Gaussian is often used for the effective source distribution. The simulated images convolved with the Gaussian + Lorentzian function result in the minimum RMS of the residuals for both the lower and higher probe currents, suggesting the plausibility of the Gaussian + Lorentzian function as the effective source distribution. The best FWHM for the higher probe current is larger than that for the lower probe current, which is consistent with the fact that increasing the incident probe current is equivalent to enlarging the source image on the specimen. Assuming that the experimental conditions such as the accelerating voltage and convergence semi-angle are the same, however, it is expected that a 4-fold decrease in probe current will halve the FWHM (probe diameter) on the basis of the definition of the brightness given later. Nevertheless, the optimum FWHM of 80 pm for the experimental conditions in Fig. 3a is only 20% less the FWHM of 100 pm in Fig. 3b. This disagreement suggests that there is probe spreading due to disturbances that are independent of the demagnification ratio of the electron source.

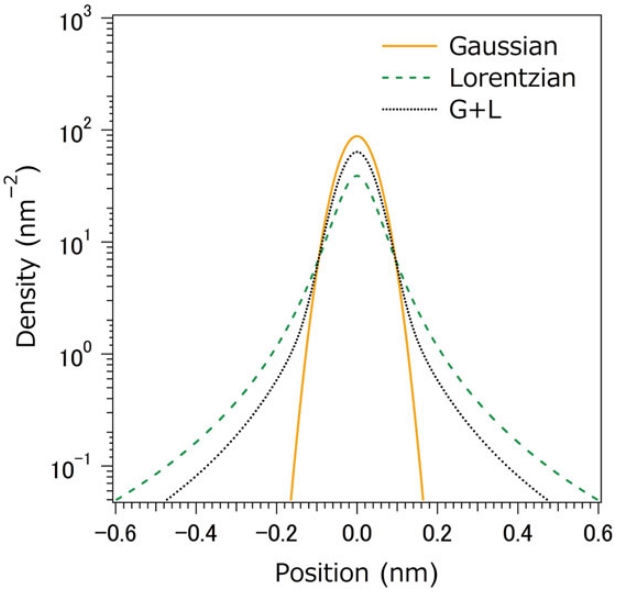

Fig. 2. Comparison of three distribution functions used to represent the effective source distribution, whose FWHMs were set to 100 pm. G + L, Gaussian + Lorentzian function.

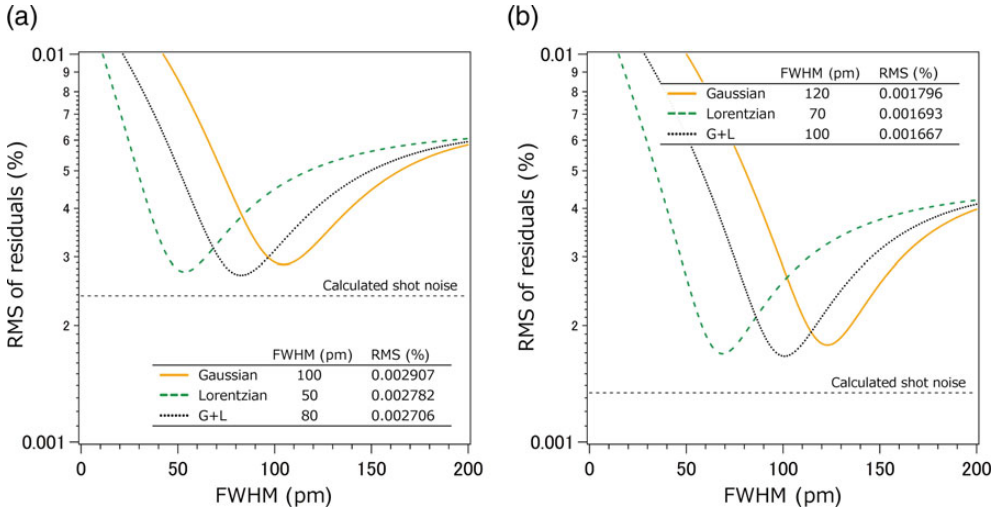

Fig. 3. RMS of the residuals for each distribution function as a function of the FWHM. (a) and (b) correspond to the lower and higher probe currents, respectively. The inset tables show the optimum FWHM and the corresponding RMS of the residuals for each distribution function. The broken horizontal lines indicate the theoretical shot noises, which were calculated on the basis of the Poisson process and the ideal DQE of the signal detection system.

Now, we estimate the magnitude of the shot noises in the experimental images by considering the number of electrons at each pixel. The probability of occurrence of shot noises can be described by a Poisson process. Provided that the number of detected electrons is X, the standard deviation of the number of shot noises is assumed to be the square root of X if the detective quantum efficiency (DQE) of the signal detection system is ideal (i.e., unity). Note that we can directly obtain the number of detected electrons at each pixel using the quantitative contrast Q_{ADF}, because it corresponds to the fraction of incident probe electrons, which can be obtained using the measured probe current, the dwell time per image and the number of images used in summation. Using the simulated images convolved with the Gaussian + Lorentzian function at the optimum FWHM, we calculated the theoretical shot noises under the above conditions. The calculated shot noises are represented as broken horizontal lines in Fig. 3. These results indicate that ~80% of the RMS of the differences between the experiment and simulation is accounted for by the random shot noises in the experimental images.

Next, we investigate the two-dimensional differences between the experimental and simulated images. Figure 4a and b corresponds to the lower and higher probe currents, respectively, where the experimental and simulated images are shown in the upper rows, and the corresponding residual images are shown in the lower rows. The optimum convolution kernels are shown as insets in the upper rows; only the central part of each kernel is displayed and its intensity scale is set in the same range. The corresponding

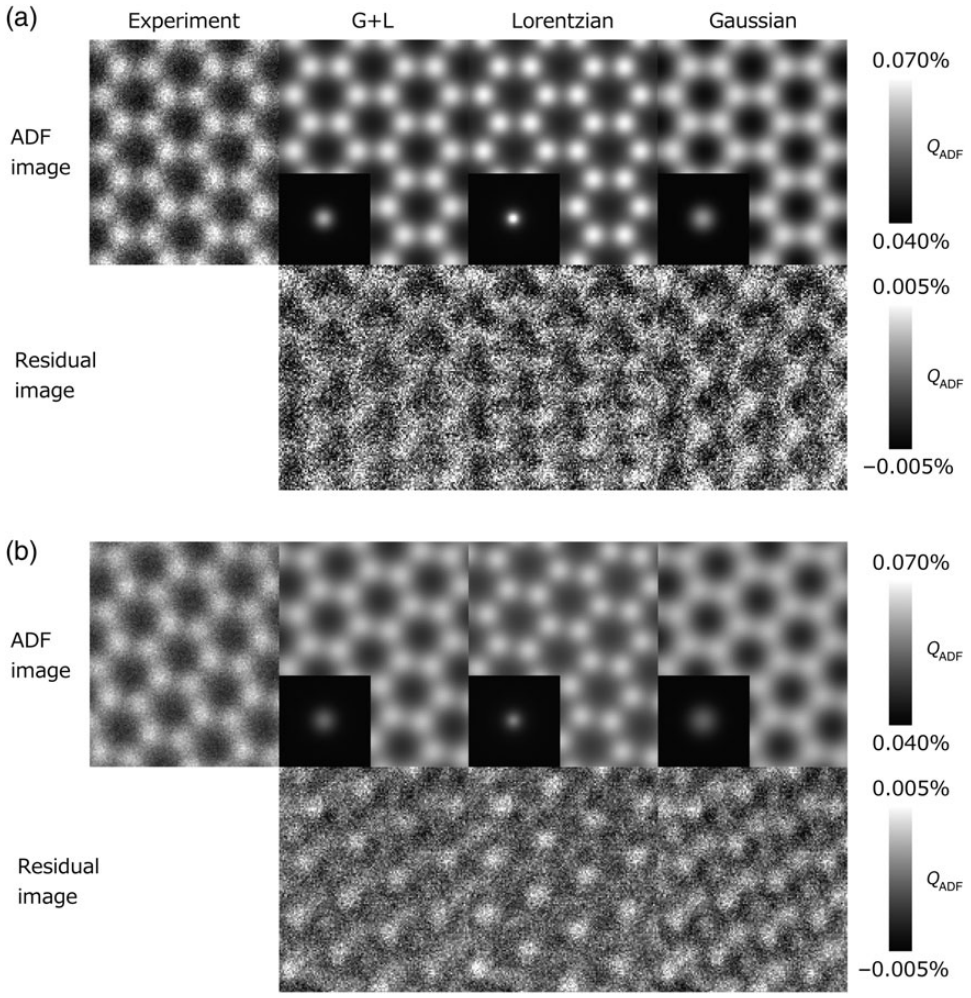

Fig. 4. Experimental and simulated ADF images using each optimized distribution function (upper rows) and corresponding residual images (lower rows). The image area is $0.83 \times 0.99\ \mathrm{nm}^2$. The FWHMs for the lower probe current (a) are 80, 50 and 100 pm for the Gaussian + Lorentzian, Lorentzian and Gaussian, respectively. For the higher probe current (b), the FWHMs are 100, 70 and 120 pm for the Gaussian + Lorentzian, Lorentzian and Gaussian, respectively. The quantitative contrast scales for the ADF and residual images are set in the ranges of 0.04–0.07 and −0.005–0.005%, respectively. The insets in the upper rows show the central part of each convolution kernel, where the intensity scale is set in the same range.

quantitative contrast scales for the ADF and residual images are shown on the right side. It should be noted that the scales for the residual images are set in the small range of −0.005 to 0.005% to highlight the subtle residuals. In the Gaussian-convolved images, the residual images show well-defined features. Thus, it is clear that the Gaussian-convolved images cannot explain the experimental images. In contrast, the simulated images convolved with the Gaussian + Lorentzian function show better agreement with the experimental images. These results are consistent with those for the RMS of the residuals shown in Fig. 3. Note that the residual images in Fig. 4b show the patterns differ from the intrinsic hexagonal structures of graphene. These patterns cannot be explained by the effective source distribution or an aberration such as a spherical aberration or 2-fold astigmatism. One of the probable causes is the residual aberration such as a coma aberration or 3-fold astigmatism.

To investigate the remaining residuals in detail, we compared the line profiles extracted along the C–C pairs, as shown in Fig. 5, where (a) and (b) correspond to the lower and higher probe currents, respectively. To reduce the effects of the shot noises in the experimental images, we took the average of four and three line profiles for (a) and (b), respectively, each of which is an average over three pixels, corresponding to ~0.02 nm. As shown in Figs. 4 and 5, the best-fitted Gaussian-convolved images show a higher quantitative contrast Q_{ADF} between the C–C pairs but a lower Q_{ADF} at the center of the six-membered ring than the experimental images. The Gaussian with a smaller width could give a better fit to the experimental Q_{ADF} between the C–C pairs, but the convolved Q_{ADF} at the center of the six-membered ring becomes lower, because the Gaussian decreases rapidly, as shown in Fig. 2. In contrast, the Lorentzian and Gaussian + Lorentzian functions show better agreement with experimental profiles. According to the RMS of the residuals in Fig. 3, however, we concluded that the Gaussian + Lorentzian-convolved images most accurately reproduce the experimental images in this study.

In the experimental profiles in Fig. 5, the asymmetry between two carbon peaks is noticeable, and this asymmetry corresponds to the patterns being different from the intrinsic hexagonal structures of the graphene shown in Fig. 4b. In this study, although we incorporated residual geometrical aberrations up to the fifth order into the simulations, the intensity asymmetries at the C–C pairs were not reproduced in the simulated images. These asymmetries may be due to a time-dependent aberration (coma or 3-fold astigmatism) as mentioned above. There is a possibility that the RMS of the residuals can be decreased further by optimizing independently the FWHMs of Gaussian and Lorentzian, and the contribution of the Lorentzian in the Gaussian + Lorentzian function. However, further optimization of the convolution conditions was not attempted, since the 80% of the residuals was accounted for by the random shot noises in the experimental images.

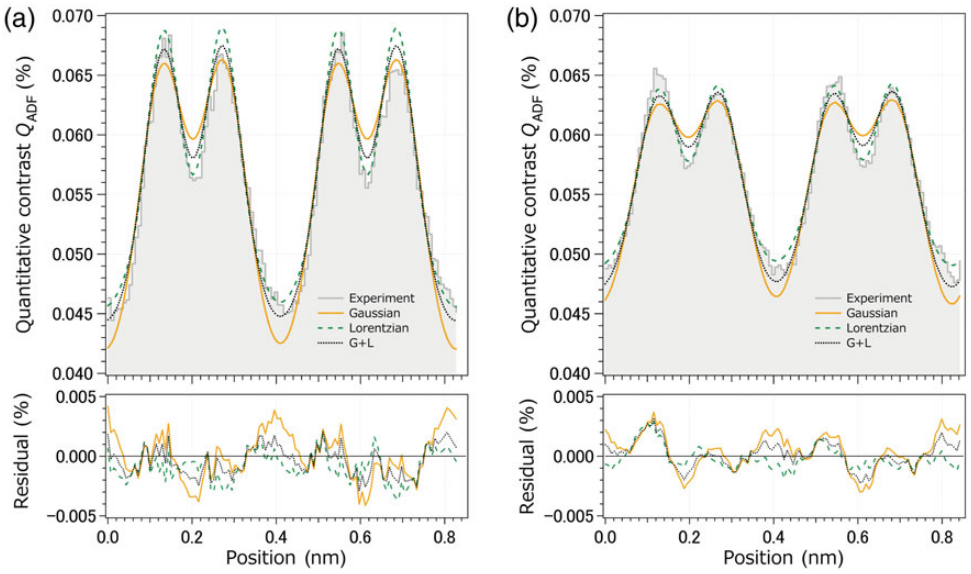

Fig. 5. Line profiles extracted along the C–C pairs in experimental and convolved images for each distribution function. Corresponding residual profiles are shown at the bottom. The FWHMs for the lower probe current (a) are 80, 50 and 100 pm for the Gaussian + Lorentzian, Lorentzian and Gaussian, respectively. For the higher probe current (b), the FWHMs are 100, 70 and 120 pm for the Gaussian + Lorentzian, Lorentzian and Gaussian, respectively. The line profiles are averages of four and three line profiles for (a) and (b), respectively, each of which is an average over three pixels, corresponding to ~0.02 nm.

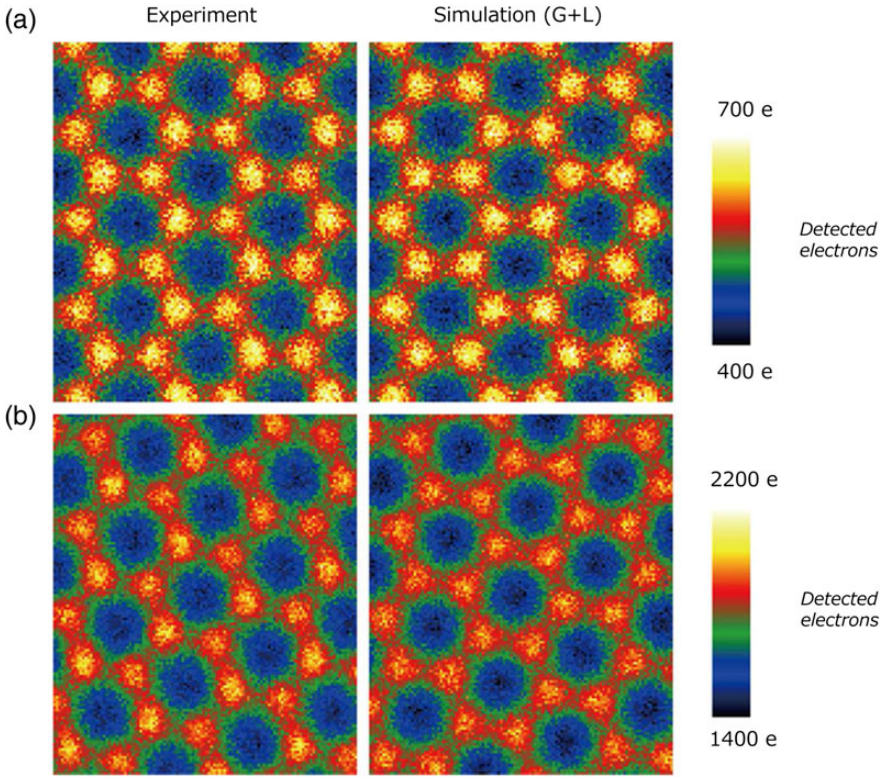

Fig. 6. Comparison of experimental images with the simulated images after Gaussian + Lorentzian convolution, where the shot noises were added on the basis of the Poisson process. The scales shown on the right side represent the number of detected electrons at each pixel. The FWHMs for the Gaussian + Lorentzian functions are 80 and 100 pm for the (a) lower and (b) higher probe currents, respectively.

By virtue of the quantitative analyses, we can experimentally evaluate the brightness of the electron source. The brightness is defined by Eq. (5), in which I_0, α and F represent the probe current, the convergence semi-angle of the probe and the FWHM, respectively.

$$\text{Brightness} = \frac{I_0}{\pi(F/2)^2\pi\alpha^2}. \qquad (5)$$

Assuming a round source whose diameter is the FWHM of the optimized distribution function (G + L), the calculated brightnesses [A cm^{-2} sr^{-1}] for the lower and higher probe currents are 2.0×10^8 and 4.8×10^8, respectively. These values are roughly equal to that (5.6×10^8) reported by the manufacturer, although this evaluation strongly depends on the assumed distribution function. Since the extraction voltage and the temperature of the electron source were constant in this study, the brightness should not depend on the probe current nor on the demagnification of the electron source, while the effective brightness may have been reduced by the above-mentioned practical disturbances.

Finally, Fig. 6 shows a comparison of the experimental images with the best-fitted simulated images. The latter are Gaussian + Lorentzian-convolved images with the optimum FWHMs, where the shot noises were introduced on the basis of the Poisson process. Figure 6a and b corresponds to the lower and higher probe currents, respectively. The scales shown on the right side represent the number of detected electrons at each pixel. The convolved images exhibit excellent agreement with the experimental images. The number of detected electrons in Fig. 6a is less than 700 per pixel, which means that only a few electrons are detected per pixel of each image during the multiple acquisitions. This result demonstrates that truly quantitative ADF imaging with high accuracy and sensitivity was realized, where even a single electron can be detected. Moreover, the real-space comparison between the experimental and simulated images confirmed that the effective source distribution is more likely to be the Gaussian + Lorentzian function, not the simple Gaussian. The effective source distribution also includes the effects of mechanical and electrical instabilities associated with the instrument [10]. The accurate measurement of the effective source distribution and its appropriate inclusion into simulations are indispensable for quantitative ADF imaging to realize the atom-by-atom analysis of crystals or nonperiodic structures, which may include interfaces or impurity atoms.

Concluding remarks

We have achieved the quantitative observations and analyses of atomic-resolution ADF images using a single-layer graphene. A single-layer graphene specimen is crucial in this quantitative study because of its clear crystal structure with no uncertainties such as an amorphous surface layer due to ion thinning or contamination as well as the specimen thickness, which was an unknown parameter in conventional quantitative studies. High S/N ratio ADF images of the single-layer graphene were obtained without image distortion using multiple fast acquisitions and drift correction techniques. The ADF intensities were converted into quantitative contrast, where the nonlinear response of the signal detection system was fully taken into account. Thus, we could quantitatively compare the experimental images with the simulated images that include geometrical aberrations (up to the fifth order), a defocus spread and an effective source distribution. By considering the RMS of residuals between the experimental and simulated images, we found that the experimental images can be more adequately explained by using a Gaussian + Lorentzian function as the effective source distribution than by using a simple Gaussian. The quantitative analyses also suggest that the main factors contributing to the residuals are the shot noises and other residual aberrations. The visibility of atoms in quantitative ADF images strongly depends on the probe current, suggesting the importance of a high-brightness electron source. We can also evaluate the brightness of the electron source based on the FWHM of the effective source distribution. Thus, this study is useful for not only material characterization but also the evaluation of microscope performance characteristics.

Acknowledgements

We thank Dr Suenaga for providing the graphene specimen and encouragement. We also thank Drs van Cappellen, Inoke, Matsumoto, Jian and Freitag for the precise alignment of our Titan^3 microscope with DCOR.

Funding

This study was supported by the JST Research Acceleration Program and the Nanotechnology Platform of MEXT, Japan. Funding to pay the Open Access publication charges for the article was provided by National Institute for Materials Science.

References

1. Pennycook S J, Jesson D E (1991) High-resolution Z-contrast imaging of crystals. *Ultramicroscopy* 37: 14–38.
2. LeBeau J M, Stemmer S (2008) Experimental quantification of annular dark-field images in scanning transmission electron microscopy. *Ultramicroscopy* 108: 1653–1658.
3. Ishikawa R, Lupini A R, Findlay S D, Pennycook S J (2014) Quantitative annular dark field electron microscopy using single electron signals. *Microsc. Microanal.* 20: 99–110.
4. Yamashita S, Koshiya S, Ishizuka K, Kimoto K (2015) Quantitative annular dark-field imaging of single-layer graphene. *Microscopy* 64: 143–150.
5. Ishikawa R, Lupini A R, Findlay S D, Taniguchi T, Pennycook S J (2014) Three-dimensional location of a single dopant with atomic precision by aberration-corrected scanning transmission electron microscopy. *Nano Lett.* 14: 1903–1908.
6. Dwyer C, Erni R, Etheridge J (2010) Measurement of effective source distribution and its importance for quantitative interpretation of STEM images. *Ultramicroscopy* 110: 952–957.
7. Dwyer C, Maunders C, Zheng C L, Weyland M, Tiemeijer P C, Etheridge J (2012) Sub-0.1 nm-resolution quantitative scanning transmission electron microscopy without adjustable parameters. *Appl. Phys. Lett.* 100: 191915.
8. Nguyen D T, Findlay S D, Etheridge J (2014) The spatial coherence function in scanning transmission electron microscopy and spectroscopy. *Ultramicroscopy* 146: 6–16.
9. LeBeau J, D'alfonso A, Findlay S, Stemmer S, Allen L (2009) Quantitative comparisons of contrast in experimental and simulated bright-field scanning transmission electron microscopy images. *Phys. Rev. B* 80: 174106.
10. LeBeau J, Findlay S, Wang X, Jacobson A, Allen L, Stemmer S (2009) High-angle scattering of fast electrons from crystals containing heavy elements: simulation and experiment. *Phys. Rev. B* 79: 214110.
11. LeBeau J M, Findlay S D, Allen L J, Stemmer S (2010) Standardless atom counting in scanning transmission electron microscopy. *Nano Lett.* 10: 4405–4408.
12. Rosenauer A, Gries K, Muller K, Pretorius A, Schowalter M, Avramescu A, Engl K, Lutgen S (2009) Measurement of specimen thickness and composition in $Al_xGa_{1-x}N/GaN$ using high-angle annular dark field images. *Ultramicroscopy* 109: 1171–1182.
13. Kim S, Oshima Y, Sawada H, Kaneyama T, Kondo Y, Takeguchi M, Nakayama Y, Tanishiro Y, Takayanagi K (2011) Quantitative annular dark-field STEM images of a silicon crystal using a large-angle convergent electron probe with a 300-kV cold field-emission gun. *J. Electron Microsc.* 60: 109–116.
14. Maunders C, Dwyer C, Tiemeijer P C, Etheridge J (2011) Practical methods for the measurement of spatial coherence—a comparative study. *Ultramicroscopy* 111: 1437–1446.
15. Verbeeck J, Beche A, Van Den Broek W (2012) A holographic method to measure the source size broadening in STEM. *Ultramicroscopy* 120: 35–40.
16. Kimoto K, Ishizuka K, Asaka T, Matsui Y (2006) Software techniques for high-accuracy in STEM imaging. In: *Proceedings of the 16th International Microscopy Congress, Vol. 2*, 609 p.
17. Kimoto K, Xie R-J, Matsui Y, Ishizuka K, Hirosaki N (2009) Direct observation of single dopant atom in light-emitting phosphor of β-SiAlON:Eu^{2+}. *Appl. Phys. Lett.* 94: 041908.
18. Kimoto K, Asaka T, Yu X, Nagai T, Matsui Y, Ishizuka K (2010) Local crystal structure analysis with several picometer precision using scanning transmission electron microscopy. *Ultramicroscopy* 110: 778–782.

19. Ishizuka K (2002) A practical approach for STEM image simulation based on the FFT multislice method. *Ultramicroscopy* 90: 71–83.
20. Weickenmeier A, Kohl H (1991) Computation of absorptive form factors for high-energy electron diffraction. *Acta Crystallogr. Sec. A* 47: 590–597.
21. Tewary V, Yang B (2009) Singular behavior of the Debye–Waller factor of graphene. *Phys. Rev. B* 79: 125416.
22. Findlay S D, LeBeau J M (2013) Detector non-uniformity in scanning transmission electron microscopy. *Ultramicroscopy* 124: 52–60.